The irradiance instrument subsystem (IRIS) on the airborne-lunar spectral irradiance (air-LUSI) instrument

Steven E Grantham[1,*] ⦿**, Kevin R Turpie**[2] ⦿**, Thomas C Stone**[3] ⦿**, S Andrew Gadsden**[4] ⦿**, Thomas C Larason**[1] ⦿**, Clarence J Zarobila**[1] ⦿**, Stephen E Maxwell**[1]**, John T Woodward**[1] ⦿ **and Steven W Brown**[1] ⦿

[1] The National Institute of Standards and Technology, Gaithersburg, MD 20899, United States of America
[2] The University of Maryland Baltimore County, Baltimore, MD 21250, United States of America
[3] US Geological Survey, Flagstaff, AZ 86001, United States of America
[4] McMaster University, Hamilton, ON L8S 4L7, Canada

E-mail: grantham@nist.gov

CrossMark

Abstract

The objective of the airborne lunar spectral irradiance (air-LUSI) project is to make low uncertainty, SI-traceable measurements of the LUSI in the visible to near-infrared region from an aircraft above most of the optically absorbing components of the atmosphere. The measurements are made from a NASA ER-2 aircraft, which can fly at altitudes of approximately 20 km above sea level. Air-LUSI measurements, corrected for residual atmospheric attenuation, are designed to provide a matrix of low uncertainty top-of-the-atmosphere lunar irradiances at known lunar phase and libration angles to be compared and combined with other lunar irradiance data sets to constrain the uncertainties in models of lunar irradiance and reflectance. The measurements are also expected to provide insight into the differences between models and satellite sensor measurements of lunar irradiance. This paper describes the development and characterization of the air-LUSI subsystem for acquiring lunar measurements, called the irradiance instrument subsystem, prior to flight.

Keywords: optics, lunar spectral irradiance, satellite calibration

(Some figures may appear in color only in the online journal)

1. Introduction

Reliable *in situ* calibration of on-orbit sensors is one of several key requirements to achieve the science objectives identified for current and future Earth Observing missions. Historically, sensors have used celestial targets such as the Sun and the Moon along with Pseudo-Invariant Calibration Sites on the Earth [1, 2] for trending responsivity changes on-orbit. Each approach has limitations and no single approach fully addresses a sensor's *in situ* vicarious calibration requirements.

The Moon is an attractive exo-atmospheric calibration target for space-based sensors that observe the Earth because the lunar surface is photometrically stable [3], flux levels approximate those from the Earth, and no atmospheric corrections need to be applied to the measurements [4–6]. While many sources of uncertainty that arise when vicariously calibrating sensors using Earth targets are eliminated, lunar measurements are complicated because the lunar irradiance is a function of the relative positions of the Sun, Moon, and observer (spacecraft).

The United States Geological Survey (USGS) has developed the robotic lunar observatory (ROLO) model of the top-of-the-atmosphere (TOA) lunar reflectance, which accounts for changes in lunar irradiance as a function of viewing conditions [5]. The USGS ROLO model and the Global Space-based Inter-Calibration System Implementation of the ROLO model (the GIRO model) [7, 8] represent the current most precise knowledge of lunar spectral reflectance. The current uncertainties in the ROLO model cannot be demonstrated to better than ~5%, with a 3% to 4% uncertainty component coming from the atmospheric transmittance used in the stellar-based calibration of the ROLO telescope [9]. Differences between sensor measurements of the lunar irradiance and the ROLO Model can be 10% and greater [10, 11]. Furthermore, the ROLO model is not traceable to the International System of Units (SI).

The airborne lunar spectral irradiance (air-LUSI) mission has four objectives: (a) fly an instrument above 90% of the Earth's atmosphere on a high-altitude ER-2 aircraft; (b) demonstrate the ability to track the Moon; (c) develop the capability to make SI-traceable, LUSI measurements with uncertainties on the order of 0.5%; and (d) through these high-altitude aircraft measurements, improve the current knowledge of LUSI to benefit calibration-sensitive Earth observations. A longer-term goal of this program is to integrate the suite of low uncertainty lunar irradiance measurements made by air-LUSI with other programs that actively measure the lunar irradiance to facilitate development of a revised SI-traceable lunar model. While it is an objective of the air-LUSI program to measure the lunar irradiance with a combined standard uncertainty of 0.5% or less, SI-traceable, TOA lunar irradiance measurements with uncertainties around 1% would enable distinction between uncertainties in the ROLO model and uncertainties in instruments' lunar irradiance measurements.

Principal considerations leading to the decision to make lunar measurements from an ER-2 aircraft at altitudes higher than 20 km include: 1. At those altitudes, the measurements will be above 90% of the atmosphere, much closer to direct exo-atmospheric LUSI measurements than mountain-top measurements, for example. Propagation from the measurement altitude to the TOA can be modeled with uncertainties less than 1%, eliminating the need for Langley measurements; and two. Calibrations of the instrument can be done before and after each flight and monitored in-flight, leading to a more complete understanding of measurement uncertainties. Figure 1 shows example modeled atmospheric transmittances from the elevation at the ROLO site in Flagstaff, AZ and from a typical expected ER-2 aircraft altitude to the TOA. Transmittances were calculated using MODTRAN with nominal slant paths and zenith angles and a 1976 US Standard Atmosphere [12] with 380 ppmv CO_2. Atmospheric attenuation in the propagation to the TOA is 5–50 times greater from an elevation of 2.15 km (the elevation of the ROLO Observatory in Flagstaff, AZ) than from the ER-2 flight at altitudes around 21.5 km, and there is no residual water vapor at 21.5 km.

This paper focuses on the development and characterization tests of the radiometric sub-system of air-LUSI, the irradiance instrument subsystem (IRIS). A description of the air-LUSI
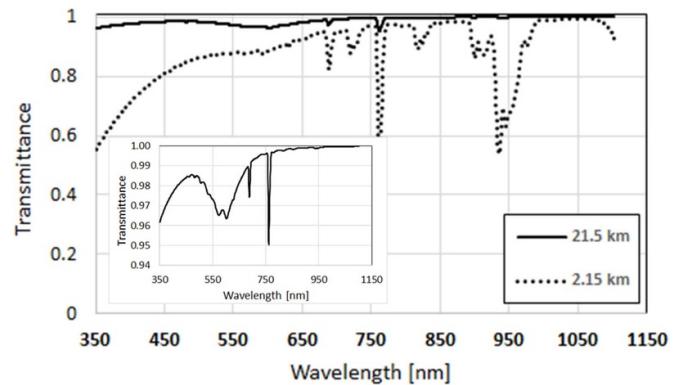

Figure 1. Atmospheric transmittances from 2.1 km and 21.5 km altitudes.

instrument is given in section 2; section 3 provides details on the characterization of IRIS's performance; and section 4 discusses estimates of the in-flight signals expected when measuring the lunar irradiance. Summary and conclusions are given in section 5.

2. Air-LUSI instrument description

Challenges of designing the air-LUSI instrument included conforming to the spatial constraints of the ER-2 wing pod, adapting to the temperature and pressure changes encountered during flight, keeping the Moon in the field-of-view during flight, ensuring that the ground calibration is maintained during data collection at altitude, and ensuring autonomous operation during flight. The air-LUSI instrument is composed of three sub-systems: the autonomous, robotic telescope mount instrument subsystem (ARTEMIS) keeps the telescope fixed on the Moon to within $\pm 0.5°$; IRIS makes radiometric measurements of the lunar irradiance; and the high-altitude ER-2 adaptation sub-system manages thermal control of the instrument.

Conceptually, IRIS emulates the design of a telescope/spectrometer system previously used for lunar irradiance measurements at the Fred Lawrence Whipple Observatory on Mt Hopkins, AZ [12, 13]. It consists of a telescope with an integrating sphere receiver at the focal plane [14]. Light is coupled from the integrating sphere to a spectrograph using a steel-jacketed fiber-optic cable. An LED source housed in the Instrument Enclosure is included to monitor the instrument's radiometric responsivity. The output of the LED source is coupled to a separate port on the integrating sphere using a 2nd optical fiber. A bare silicon photodiode mounted on the exterior sphere wall over a small hole in the sphere is used to monitor the input flux into the integrating sphere.

Air-LUSI is designed to fit in one of two wing pods on a NASA ER-2 aircraft [15]. The locations of air-LUSI components within the wing pod are shown in figure 2. Only the mid-body and the aft-body sections of the wing pod are used. The mid-body section is maintained at a temperature above 0 °C and an atmospheric pressure 25% of the pressure at sea level, corresponding to an altitude of 10 km. The mid-body provides
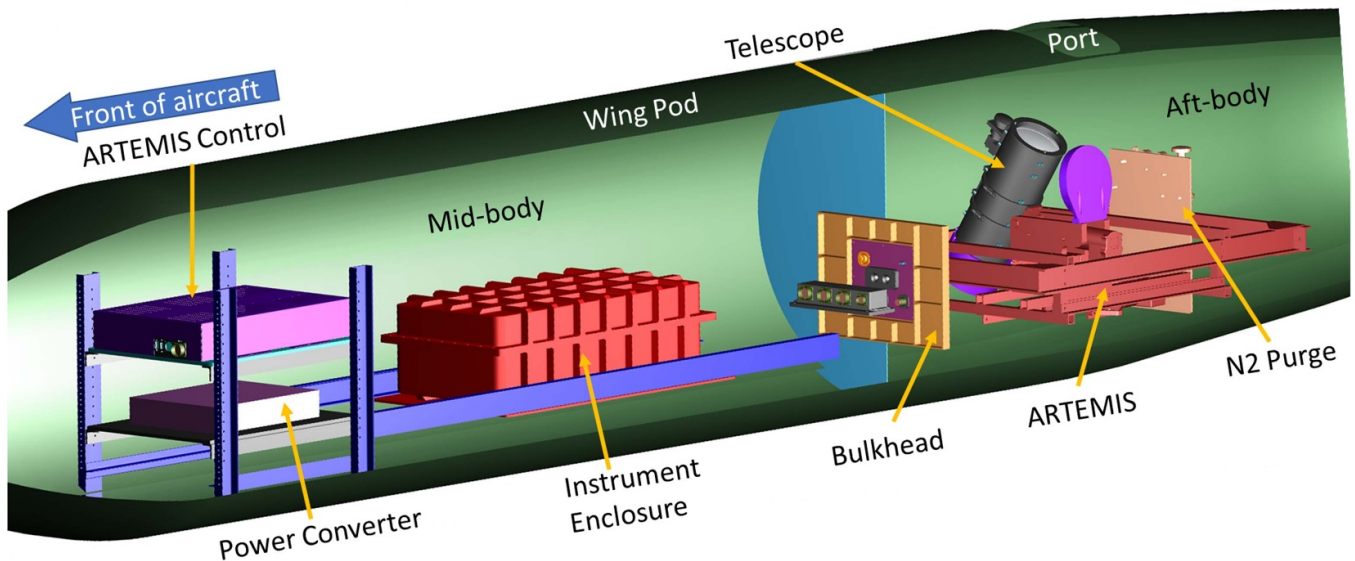
Figure 2. Layout of air-LUSI components in the wing pod of the ER-2 aircraft.

access to aircraft power, aircraft networking, and a connection to indicators and switches located in the aircraft's cockpit. A rack-mounted instrumentation plate dedicated to ARTEMIS control in the mid-body holds a small computer and the telescope control actuator power supplies. A power converter which provides 60 Hz, 120 V from aircraft power, 400 Hz, 120 V, and a distribution panel that provides the electrical interface between the instrument and the aircraft are located at the front of the mid-body in an instrument rack. The IRIS Instrument Enclosure, housing the spectrograph, the LED validation source, transimpedance amplifiers, control computer and associated equipment, is described in detail in the next section. A bulkhead with a feedthrough panel separates the mid-body from the aft-body where the IRIS telescope and the ARTEMIS frame and controlling actuators are located. Fiber optic and electrical cables run between the mid-body and the aft-body through a bulkhead panel.

Figure 3 is a schematic diagram of the IRIS telescope mounted on the ARTEMIS frame. The telescope is pointed >46° above the horizon. A nitrogen purge system, designed to keep moisture out of the telescope tube and integrating sphere receiver during descent, is shown in the back. Lunar measurements are made through a rectangular viewing port in the wing pod that is open to the atmosphere. The open port has the advantage that we do not have to account for the radiometric losses when observing through a window. Conversely, the disadvantage is that instrumentation located in the aft-body of the aircraft is exposed to ambient temperatures and pressures, approximately −60 °C and 7.2 kPa, respectively.

2.1. Description of the IRIS subsystem

Major components of IRIS are the telescope and its integrating sphere receiver, the spectrograph, a fiber bundle, an LED validation source, a data logger, control software and a
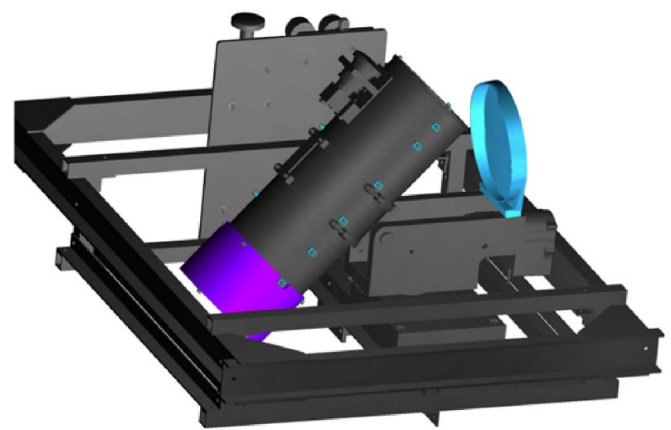

Figure 3. CAD drawing of the IRIS telescope mounted on the ARTEMIS mount. The telescope is pointed 46° above the horizon.

communications interface for interaction with the instrument during flight; details of each component are provided below. Telescope pointing and thermal management details are included as well.

2.1.1. Telescope. A telescope is used to collect moonlight which is passed to a commercial spectrometer via fiber-optics; see [14] for details on the telescope. Figure 4 is a schematic diagram of the telescope layout. Two optical fiber cables (not shown) couple to the integrating sphere receiver. One cable introduces light from an LED into the integrating sphere to monitor the system performance during flight. The 2nd collects the light from the integrating sphere (either moonlight or LED light) and transfers it to the IRIS spectrograph. A photodiode installed on the sphere wall continuously measures the total incident flux in the sphere. The integrating sphere receiver is shown attached to the telescope and by itself for clarity.
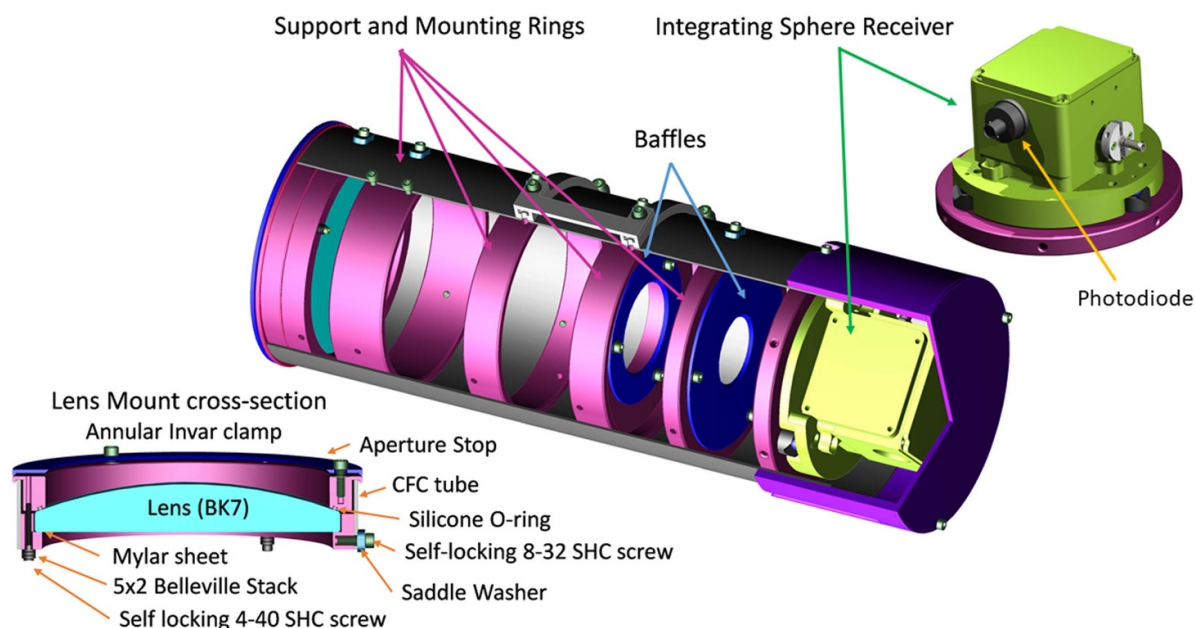
Figure 4. Schematic diagram of the IRIS telescope.

The aperture stop, fabricated from Invar 36[5], has an inner diameter of 127 mm and is located 10 mm in front of the vertex of the plano-convex receiving lens. The lens was fabricated from Schott N-BK7 optical glass and its front-surface curvature of approximately 196.1 mm was optimized for a 355 mm back focal length at the design wavelength of 530 nm. Its diameter is 139.7 mm. A simple quarter-wave optical thickness anti-reflection coating was deposited on both surfaces to improve the lens transmittance and to reduce back-reflections. Because an integrating sphere collects the light from the telescope, image quality is not critical and lens aberrations (such as spherical, field curvature, coma etc), chromatic aberrations, and defocus are not critical and do not need to be specifically corrected. Primary and secondary baffles are used to suppress stray light; a 15 mm diameter aperture serves as the field stop and defines the entrance port to the 50.8 mm diameter integrating sphere; it also sets the full field-of-view of the telescope. Figure 5 is a side view of the telescope with the tracking camera, the inertial measurement unit (IMU), and the integrating sphere receiver labelled.

2.1.2. Instrument enclosure. The instrument enclosure is located within the mid-body of the aircraft super pod. It is a clamshell style enclosure fabricated from 7075-T6 aluminum alloy. The entire enclosure is approximately 845 mm long × 419 mm wide × 257 mm tall with interior dimensions of approximately 781 mm long × 355 mm wide × 219 mm tall. The enclosure incorporates a double gasket seal to
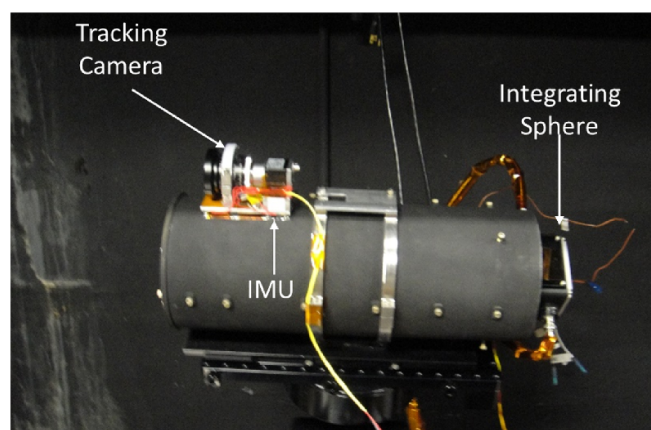
Figure 5. The air-LUSI telescope with an IMU and tracking camera mount on top.

maintain pressure during flight and 50 NAS1352-type fasteners engaged in MS21209-type locking threaded inserts to secure the lid to the bottom of the enclosure and compress the sealing gaskets. Both the lid and base of the enclosure were fabricated from a single piece of material in order to avoid potential leaks from a welded joint.

The Instrument Enclosure houses a spectrograph, an LED source with monitor photodiode, two transimpedance amplifiers, a computer and DAQ system, a pressure sensor, temperature sensor, solid-state relays, and the control computer. The spectrograph is mounted in the front of the enclosure. The other electronic instruments and components are housed toward the rear of the enclosure on a two-tiered assembly. The top tier accommodates the computer which operates control software, a USB-based digital and analog data module, and the two transimpedance amplifiers used for current-to-voltage conversion of signals from the two photodiodes. The
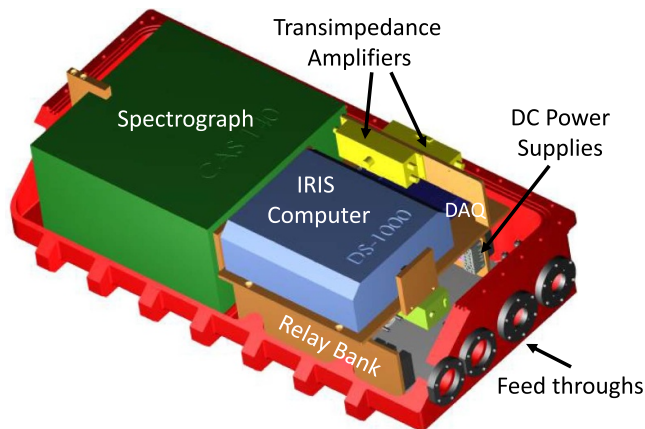
Figure 6. Schematic diagram of the instrument enclosure.

photodiode mounted in the Instrument Enclosure monitors the output power of the LED validation source. The lower tier houses the DC power supplies which provide power for the computer and electronics within the enclosure. In addition, the lower tier includes a pressure sensor and the solid-state relays for interaction with the pilot switches and indicators located in the aircraft cockpit as well as the nitrogen purge solenoid housed on the telescope mounting frame. Finally, the lower tier holds the LED validation source including the fiber launch optics, beam splitter, shutter, monitor photodiode, and LED driver electronics. A schematic diagram of the enclosure is given in figure 6.

The aft face of the enclosure accommodates four feed-throughs for signals, power, and communication. Two of these feedthroughs are fiber optic feedthroughs based on ISO KF 40 vacuum flanges and O-ring sealed via bulkhead clamps on the front face. The pressure differential encountered during flight (high pressure inside of chamber, low pressure outside of flange) is opposite to that seen under typical KF 40 flange implementations. Therefore, the bulkhead clamps were designed to provide external radial backing of the KF 40 O-rings in order to eliminate the possibility of the KF 40 O-rings coming dislodged during mid-body depressurization. The electrical feed throughs are based on elastomer sealed MS3470W22-55P and MS3470W20-16P electrical bulkhead connectors. Each feedthrough incorporates the bulkhead connector sealed with MIL-S-8802 type sealant to an O-ring sealed flange to provide a vacuum seal. The MS3470W22-55P connector provides electrical connectivity for the telescope photodiode, three external thermocouple sensors and ethernet connection to the aircraft. The MS3470W20-16P connector provides connectivity for the 120 V 60 Hz power, 28 V aircraft power, pilot switches and indicator lights, and the nitrogen purge solenoid housed on telescope mounting frame. Figure 7 is a picture of the Instrument Enclosure with the top off and loaded with instrumentation. The LED equipment that sits underneath the computer table is not visible in the image.

2.1.3. IRIS LED system for tracking potential in-flight responsivity changes.
An LED with spectral output from 450 nm

Figure 7. The instrument enclosure with the top off and loaded with instrumentation.

Figure 8. The spectral distribution of the LED and its type A uncertainty.

to 750 nm was selected as the in-flight validation source. It is rated for up to 1 A of current, giving a maximum output of 880 mW. Prior to installation the LED was seasoned for a few hundred hours until the optical output changed less than 0.1% per hour. During testing, the LED was typically run at 15%–20% of its rated current. Figure 8 shows the spectral distribution of the LED acquired by the IRIS spectrograph and the Type A measurement uncertainty with the LED current set at 200 mA.

The LED output is first collimated and input into and a large-core (600 µm), uni-fused 1×2 90%/10% fiber-optic splitter (Fibersense & Signals, Inc). The output is monitored using a photodiode coupled to the 10% output leg of the fiber splitter. The 90% leg is connected to the optical fiber that introduces the LED flux into the telescope's integrating sphere. The collimation allows the LED to be easily shuttered during data collection.

Table 1. Designation and location of four thermocouples whose readings are logged during flight. These TCs are battery operated.

Thermocouple	Location
TC1	Located inside thermal wrapping next to the optical fiber bundles
TC2	Located in the aft body to measure the ambient temperature
TC3	On the integrating sphere receiver at the end of the telescope
TC4	In the instrument enclosure on the input to the spectrograph

2.1.4. Temperature measurements. In order to accurately assess air-LUSI's status and provide necessary temperature data, thermocouple temperature sensors were installed in four parts of the instrument. The designation and locations of the four type K thermocouples are given in table 1; TCs 1, 2, and 3 reside outside of the Instrumentation Enclosure while TC4 is located at the input to the spectrograph. Their voltages are read by the data acquisition unit, or DAQ, and logged during flight.

2.1.5. In-fight control and communications. During flight, the instrument is designed to be controlled by the ER-2 pilot using four of the five available pilot switches located in the cockpit. During normal operation, the pilot can power on the instrument, initiate data collection, and shut the system down with no intervention from the ground controllers and following a simple checklist. Relays convert the 28 V signals from the aircraft routed by the switches to 5 V signals that are read by the DAQ. The pilot switches are hardwired to air-LUSI's instrumentation residing in the instrument enclosure. Switch 1 powers up the power converter to provide air-LUSI with power. This switch is activated when the aircraft is on the runway preparing for takeoff. The second switch informs the air-LUSI computer to turn the validation LED on and begin datalogging. Once air-LUSI has started data logging and all systems check out at nominal function, air LUSI turns out an indicator light in the cockpit, signaling the pilot that all systems are ready. Switch 3 is activated by the pilot when the aircraft is at altitude and at proper heading for lunar observation. Upon receiving the switch 3 signal, the air LUSI telescope is unstowed and begins tracking the Moon. Subsequent deactivation of switch 3 following lunar acquisition stows the telescope and activates the nitrogen purge to prepare the system for descent and return to the ground. Once on the ground the fourth cockpit switch is used to inform all air-LUSI systems to gracefully shut down. When shutdown is complete switches 1 and 2 are deactivated to fully depower air-LUSI.

Both ARTEMIS and IRIS send status packets to ground control over dual satellite communications systems, iridium, and inmarsat [16], via the aircraft's network. The status packets are sent approximately every second. Each IRIS downlinked status packet contains the DAQ signals for monitoring air-LUSI system operation. Every 5th spectral scan is downloaded using a remote access script over the Inmarsat downlink to monitor the spectrometer data being collected in near-real-time. Full remote control of the system over the Inmarsat link is also possible, enabling ground controllers to execute commands beyond those required for normal operation and to diagnose issues with incoming data.

2.1.6. Software. The system is controlled through a National Instruments LabVIEW™ program that processes signals from the pilot switches, passes switch state information to ARTEMIS over the aircraft network to enable tracking when needed, sends status packets to ground control, launches a utility script described below, provides data acquisition and control functions, and plots current data (if a display is connected, either directly or through remote desktop). The program can operate in two different modes, 'flight' and 'interactive.' In interactive mode, the program is responsive to user input through a Graphical User Interface; in flight mode the program is responsive to pilot switches. A utility script periodically records the time difference between the ER-2's onboard network time protocol (NTP) server and the IRIS computer local clock. Logging of the time difference was chosen over an alternative approach using built-in Windows time services to synchronize with the NTP server because the version of Windows in use pre-dates Microsoft's implementation of a subsecond precision time service [17].

The spectrograph begins acquiring data soon after power-on and continues during the entire flight. When it is not measuring the lunar spectrum in the 'At Altitude' mode (switch 3 ON), it measures the Validation Source LED (switch 3 OFF). The signals from the validation and telescope photodiodes are continuously recorded during the flight as well.

2.2. ARTEMIS pointing control

The ARTEMIS system is a simplified double gimbal system that uses machine vision to keep the Moon centered in the telescope field-of-view [18]. The ARTEMIS dimensions were constrained by the telescope dimensions, the available space in the aft-body pod, and the size of the wing pod view port. The tracking system is designed to keep the IRIS telescope pointed at the Moon to within $0.5°$ for elevation angles between $47°$ and $82°$ and azimuth angles kept between $\pm 15°$ [18–20]. Two linear industrial-grade actuators, Ultramotion A2 servocylinders, control the motion of the telescope. They were selected based on the need for tracking movements in both elevation and azimuth; the force required to reliably move the telescope with good precision and repeatability; and the environmental conditions (temperature, humidity, pressure) they would be exposed to. The telescope was designed in parallel with the ARTEMIS mount. Fitted aluminum rings hold the telescope to the ARTEMIS mount securely. Internal rings of the telescope are aligned with the mounting straps to minimize unwanted stresses on the telescope, figure 4. CAD models were shared between IRIS and ARTEMIS teams to minimize any integration issues.

Two pieces of equipment are mounted on the telescope, a tracking camera (Basler, acA1920-40um) with a lens and an IMU (VectorNav VN-100). Images from the tracking camera are used to keep the telescope aligned with the Moon. The IMU provides additional data about the aircraft such as heading, altitude and position. Finally, a nitrogen purge system was located on the ARTEMIS frame. The purge valve opens during descent and nitrogen purge gas flows through the telescope housing to mitigate potential effects of water condensation inside the telescope.

2.3. Thermal control

Thermal management and control are required for air-LUSI components located in the aft-body of the wing pod, the mid-body of the wing pod, and the optical and electrical cabling that runs from the aft-body to the mid-body of the wing pod; each has its own thermal management solution.

The IRIS telescope assembly and much of the ARTEMIS system are located in the aft-body of the wing pod, an unpressurized, unheated location within the wing pod with the possibility of significant moisture condensation during descent. The majority of the components in the IRIS telescope assembly were designed to operate in the environmental conditions expected during flight. However, the telescope's integrating sphere receiver core is fabricated from polytetrafluoroethylene (PTFE) and must maintain a temperature above the ambient atmosphere to maintain spatial stability. Phase transitions in PTFE at 19 °C and 30 °C should be accounted for in the thermal solution [21, 22]. Thermal control is accomplished by heating the unit with a 40 W thin foil polyimide heater circuit with an inline military grade thermostat (MIL-PRF-24236) set to maintain the temperature between 10 °C and 20 °C.

Several commercial off-the-shelf components within the ARTEMIS system required thermal control during flight in order to maintain device temperatures within the manufacturer's specified limits. This included the actuators, the tracking camera and the IMU. Heating is accomplished by thin foil, adhesive backed polyimide or silicone heaters. The ARTEMIS system includes a total of three heating circuits: elevation actuator, azimuth actuator and tracking camera/IMU package. While not optimally effective at the pressures expected during flight, the camera/IMU package is wrapped in multi-layer insulation (MLI) blanketing to reduce radiative heat loss during flight [23].

The fiberoptic and electrical cables in the aft-body of the wing pod can become brittle and fragile under such cold temperatures and these same temperatures can affect the optical performance of the fiber optic cables. Two separate layered cable assemblies were constructed to facilitate temperature control of the cabling. The assemblies incorporate an aluminized copper braid in order to provide a thermally conductive sleeve; the copper braid envelopes the two cable assemblies along their full length. A thermostat-controlled, silicone encased resistive heater tape circuit placed outside the

braid provides heat during flight. Finally, the assembly is wrapped in either MLI blankets (for electrical cables) or a fiberglass-insulated, PTFE-infused jacketed spiral wrap (for fiber optic cables) in order to thermally insulate the assembly. The ends of the cable assemblies are sealed with Polyimide tape with silicone adhesive suitable for low temperature applications to provide a vapor seal from the outside environment. Figure 13 shows the cable assemblies, and the telescope IS wrapped in MLI during thermal testing in the environmental chamber, discussed in section 3.2.

3. Testing and characterization

There are functional relationships between IRIS's responsivity and a number of influencing variables, including scattered light, wavelength, temperature, linearity, and temporal stability. IRIS was characterized for each of these variables as part of the development of an uncertainty budget; results of the characterizations are discussed in brief below. Development of the uncertainty budget is discussed in a separate manuscript, in preparation.

3.1. Component thermal testing in a thermal vacuum (TVAC) chamber

Prior to installing thermal controls, survivability tests of the telescope tube; the telescope with the lens installed; and integrating sphere, optical cables, and LEDs were done in a TVAC chamber. The chamber had liquid nitrogen shrouds and was capable of achieving temperatures as low as 80 K. During tests, the chamber was backfilled with approximately 66.7 Pa of nitrogen gas.

A spare telescope housing tube was placed into the environmental chamber and with pressures and temperatures expected during flight was simulated. The tube was place on a PTFE sheet on the bottom of the nitrogen shroud. Two silicon diode temperature sensors were taped to the bottom inside of the tube. Once the test was started, the temperature recorded by the silicon diodes went from 293 K to 220 K in approximately 30 min. Figure 9 shows the temperature profiles of the shroud and the two silicon temperature sensors.

Next the flight telescope, including the integrating sphere receiver and steel-jacketed optical fibers, was placed in the chamber. Teflon spacers and a Teflon sheet kept the telescope and optical fibers away from the bottom of the nitrogen shroud (figure 10). Five Si diode temperature sensors were attached at different places along the telescope tube, as shown in figure 11 (inset). These were survivability tests, and they were done with no instrumented thermal control. Consequently, no long-term soak at low temperature was attempted. The shrouds were flooded with liquid nitrogen until the shroud temperature reached 180 K. Nitrogen flow was reduced until the shroud temperature increased; nitrogen flow was again increase until the shroud temperature reached approximately 180 K again. Then the nitrogen flow was turned off and the system slowly warmed back to room temperature, figure 11. During this test,
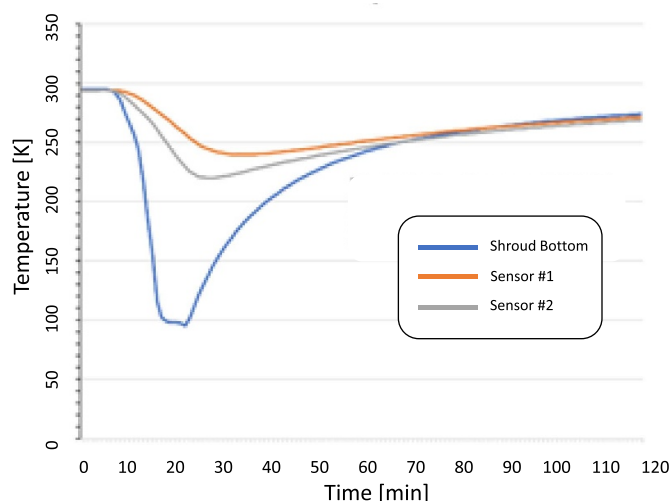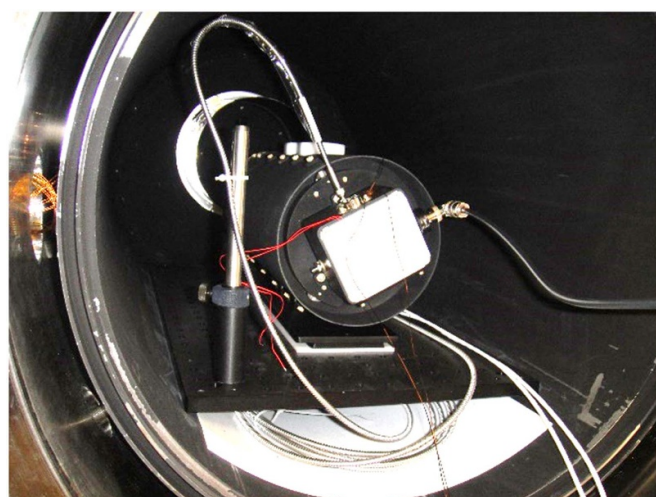
Figure 9. Telescope tube testing in the TVAC chamber.

Figure 11. Results of thermal tests of the telescope in the TVAC chamber.

Figure 10. Telescope and integrating sphere setup in the TVAC chamber.

sensor 2 went to 270 K as the shroud went to approximately 180 K.

3.2. Thermal testing in the environmental chamber

Additional thermal testing was done in a commercial environmental chamber, model ZHS-32-2H/AC from Cincinnati subzero. The chamber has a temperature range from $-34\,°C$ to $+190\,°C$ with a stability of $\pm 1\,°C$. It has a relative humidity range from 10% to 95%; the humidity was not controlled during these tests. Thermal testing in the environmental chamber was done after heaters, thermostats, MLI blankets and wrapped thermal insulation were installed. Thermal testing of the optical fiber, the telescope integrating sphere, and the IRIS spectrograph were done. The objectives of these tests were to evaluate the functionality of the heater/thermostat control, to evaluate the sensitivity of IRIS components to environmental temperatures, and to develop sensitivity coefficients
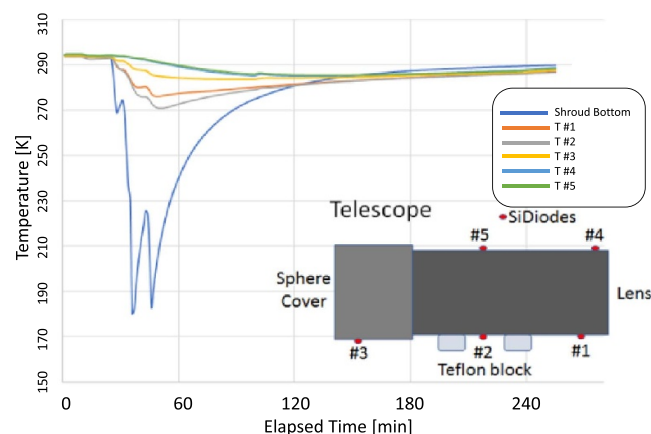
to correct for any thermal effects observed in the instrument's responsivity.

3.2.1. Thermal tests of the optical fiber. Thermal testing of the optical fiber was done to assess the effect of temperature changes on the optical fiber throughput and the effectiveness of the fiber thermal management. For this test, the instrument enclosure was placed on a table next to a small port in the environmental chamber and the optical fiber exiting the instrument enclosure was placed in the environmental chamber. The end of the fiber came out through a port on the opposite side of the environmental chamber and IRIS measured the output from a stabilized integrating sphere source (ISS). A thermocouple and thermistor were placed inside the optical fiber bundle away from the thermostat to monitor the temperature during the test. The current to the heaters from the heater power supply was also monitored.

The output of the ISS was monitored as the temperature in the environmental chamber was varied between ambient temperature ($24\,°C$) and temperatures of $0\,°C$, $-10\,°C$, $-20\,°C$ and $-30\,°C$. The temperature measured inside the fiber bundle was $0\,°C$ at an environmental chamber setpoint of $-10\,°C$. At an environmental chamber temperature of $-30\,°C$, the temperature measured inside fiber bundle was $-14\,°C$. As illustrated in figure 12, the signal measured by IRIS was observed to change by a few tenths of a percent across the temperature range. The dip observed near 950 nm is a water feature and may indicate condensation on the fiber tip. For these tests, the fiber bundle was not wrapped in a fiberglass-insulated, PTFE-infused jacketed spiral wrap as described in section 2.3, but in an MLI blanket. In subsequent fiber heater evaluation tests the fiberglass-insulated, PTFE-infused jacketed spiral wrap performed significantly better with temperatures reaching $6\,°C$ at an environmental chamber temperature of $-34\,°C$.

3.2.2. Thermal characterization of the telescope integrating sphere receiver in the environmental chamber. The goals of this test were to evaluate heater function and the telescope
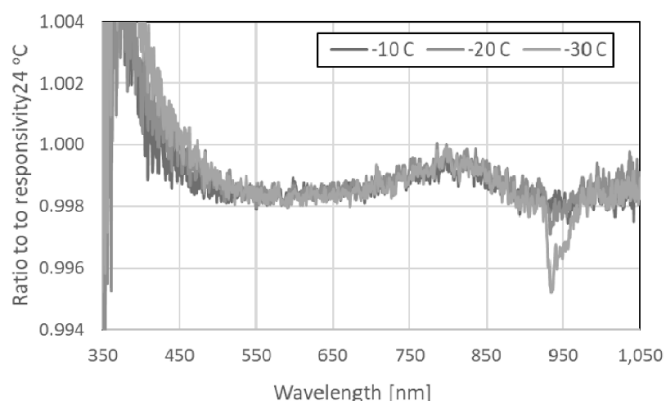
Figure 12. Results of thermal tests of the optical fiber.

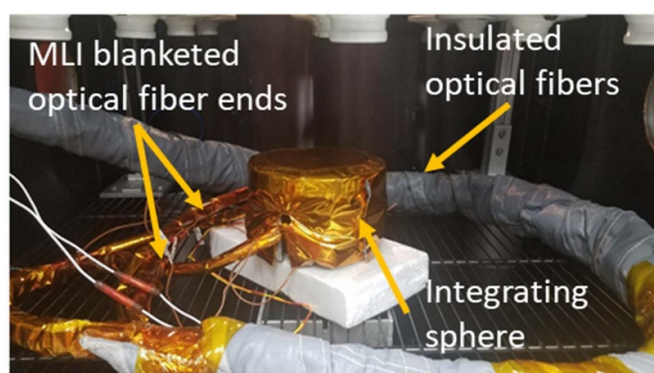**Figure 14.** TC3 temperature during thermal testing.

Figure 13. Picture of the IS setup in the environmental chamber.

receiver throughput as a function of ambient temperature, in particular looking for potential effects from the PTFE phase transition near 20 °C [21, 22]. Thermocouple TC3 was mounted on the integrating sphere's aluminum housing and its temperature was continuously logged. The LED source was turned on during testing and data were logged. To look for possible thermal dependencies, the spectrograph data were integrated over the spectral range from 500 nm to 650 nm.

Figure 13 is a picture of the IRIS integrating sphere receiver setup in the environmental chamber. The integrating sphere was installed in its housing, wrapped in MLI blankets. Both fiber inputs are visible, also wrapped in MLI blanketing near the integrating sphere connections. The insulated PTFE infused jacketed spiral wrap is shown in grey. Thermal testing of the telescope receiver throughput was done at the following 60 min long temperature plateaus: 24 °C, 5 °C, −20 °C, −34 °C, and 24 °C. Figure 14 shows the TC3 temperature as a function of elapsed time. The sawtooth pattern reflects the thermostat turning on the heaters at 5 °C and off at 15 °C; note that there is a 5 °C difference between TC3 reading and the thermostat readings. The conclusion from these tests was that the thermostat/heater system worked as designed.

3.2.3. IRIS spectrograph characterization in the environmental chamber.
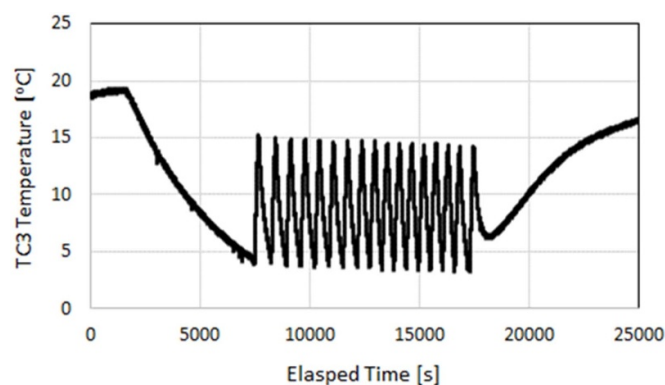The spectrograph was placed in the environmental chamber and its optical fiber went through a

small port in the chamber wall and was aligned to a lamp-illuminated integrating sphere located just outside the chamber. A second spectrograph monitored the output of the integrating sphere to correct for any changes during testing. At each temperature setting, measurements were made at least an hour after reaching a thermal plateau. For the thermal characterization, the temperature was varied between 10 °C and 35 °C (close to the 15 °C–35 °C range specified by the manufacturer) and recorded using the chamber instrumentation, a separate thermo-hygrometer, and thermocouple TC4 mounted on the input connection of the spectrograph. The spectrograph wavelength scale and responsivity were found to be functions of the ambient temperature setting. During thermal profiling, measurements of HgNe and Ne emission line pen lamps were made at each temperature setting and were used to establish the temperature dependence of the wavelength scale. The wavelength scale shifted by 0.2 nm for a 5 °C change in the environmental chamber temperature setting.

In addition, changes in the spectrograph responsivity were correlated with thermocouple TC4 temperatures. This relationship is explored further in section 3.3.

3.3. Radiometric characterization

A suite of tests was conducted on the IRIS system in order to characterize the radiometric performance of IRIS. This included measurements of linearity, scattered light effects, wavelength scale, spectrograph temperature effects, and temporal stability. The results of these measurements are discussed in the following sections.

3.3.1. Linearity.
The linearity of detectors can be measured with several different techniques. A common technique is to insert attenuating filters into the optical path to generate different optical power levels at the detector. The nonlinearity is measured as a difference from the expected response for a particular incident power and attenuation. The linearity has been evaluated using the NIST Beam Conjoiner [24–26]. In the NIST Beam Conjoiner, an input beam is separated into two paths, each path passes through a neutral density filter wheel and is recombined before passing through a third filter wheel and falling on the detector, as shown in figure 15. Typically, the
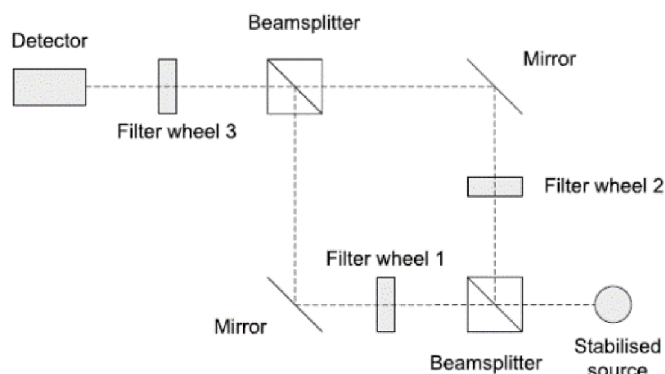
Figure 15. Schematic diagram of the flux addition method used at NIST.

input flux is varied over several decades. The method assumes that the flux from the source remains constant during all measurements and that the output flux at the detector is the sum of the fluxes along the two different paths. The ordering of the flux levels is randomized to ensure that any drift in the source maps to scatter in the measurement set and does not contribute to a trend. Filter wheels 1 and 2 each had five positions one of which was opaque and the other were neutral density filters. Filter wheel 3 had six positions, one of which was opaque. This allowed for 120 different non-zero flux levels which were simultaneously fit to yield the neutral density filter ratios and non-linearity in the detector. No *a priori* knowledge of the ND filter densities is required. In practice, several sets of spectra were taken at every combination of filters in the beam paths.

The signal from the spectrograph is recorded as a digital number (DN) and ranges in value from 0 to 32 768. The recorded signal level on the beam conjoiner varied by less than 2% across a 70-pixel band from 620 nm to 675 nm. The mean of the counts in this band were used as the signal level for each filter combination. Data below 100 DN were not included in the linearity correction because of insufficient signal-to-noise. The linearity correction was applied to all pixels of the spectrograph. The uncertainty in the linearity correction is 0.02%. The linearity corrections from the beam conjoiner are compared with the instrument vendor corrections in figure 16. Using the instrument manufacturer's convention, the linearity correction factor near the high end of the count range is 1 and the corrections at lower count levels are relative to 1.

3.3.2. Scattered light. When a spectrograph views a monochromatic source, an image of the entrance slit is formed on a detector array at the focal plane of the instrument. The array response is the instrument's line shape function (LSF) at the excitation wavelength. As the input wavelength changes, the image moves across the focal plane and a 2D matrix of LSFs can be developed. Ideally, the image of the entrance slit formed on the detector array agrees with the instrument's expected bandpass at the excitation wavelength. In a practical spectrograph system, however, the image is modified by the presence of scattered light originating from optical elements in the spectrograph.
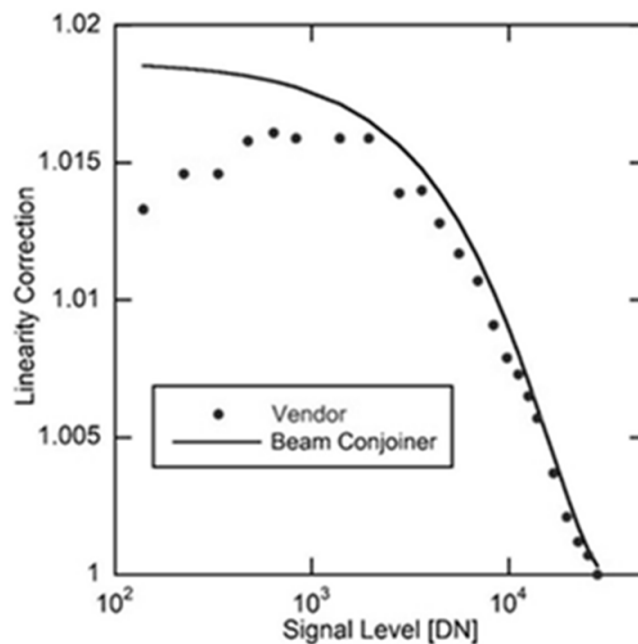

Figure 16. Linearity corrections from NIST and the instrument vendor. The second order polynomial fit is to the NIST measurements.

Accounting and correcting for scattered light in spectrometers and spectrographs have been long-standing issues in radiometry and different approaches have been tried over the years [27–29]. To correct for stray light in the IRIS spectrograph, we rely on an algorithm that corrects for an instrument's response to improperly imaged flux falling on the detector array based on measurements of the instrument's LSFs [28]. Developing the LSF matrix and nulling the properly focused radiation within the LSFs, called the In-band region, results in a matrix of improperly imaged contributions to the instrument's responsivity. This matrix, known as the stray light distribution function (SDF), describes the contribution of improperly imaged radiation in the spectrograph to its responsivity.

To generate the SDF matrix for IRIS, LSF's were measured approximately every 5 nm across the array, from 310 nm to 1090 nm. To measure the LSFs, light from a kilohertz pulsed OPO system (Ekspla, NT242) was introduced into an integrating sphere. Ideally, IRIS's flight integrating sphere would be used for these tests in order to accurately capture any influence of UV-induced fluorescence of the sphere wall material. The IRIS flight integrating sphere was unavailable for the measurements detailed here so it is planned to repeat these measurements with the flight integrating sphere at a future date. Radiant flux from the integrating sphere was measured by the IRIS spectrograph while the wavelength of the laser light was measured using a laser spectrum analyzer (LSA). An interpolation routine used the measured LSFs to generate LSFs that result in self-consistent wavelength assignments for each pixel for pixels lying between measured LSFs. A subset of normalized LSFs are shown in figure 17; figure 18 shows the SDF matrix generated from the LSF matrix.
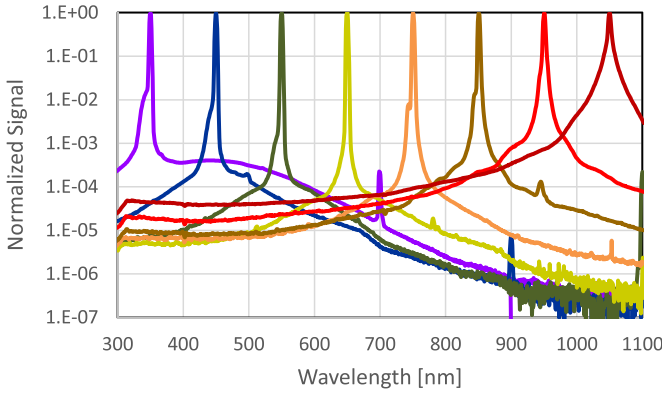
Figure 17. A subset of normalized LSFs used to develop the stray light correction matrix.
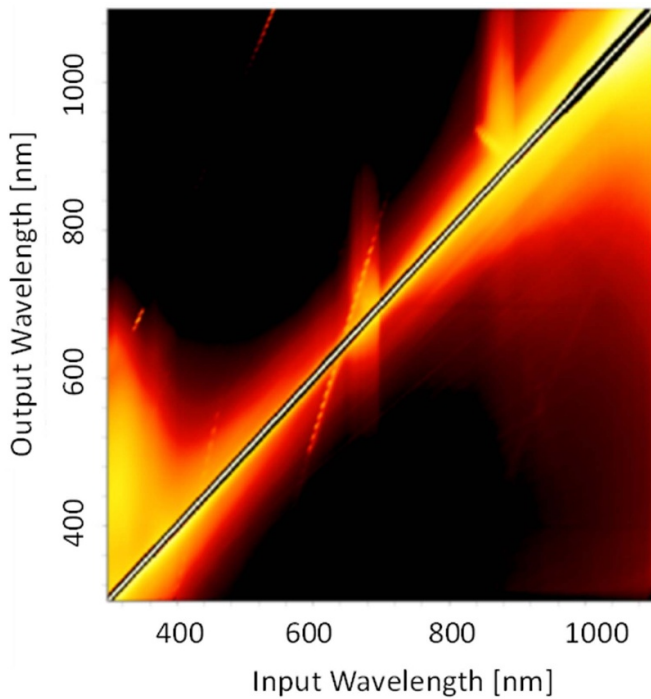

Figure 18. The SDF matrix of the scattering properties of the spectrograph.

From [28], a matrix is generated to correct measurements for this improperly imaged radiation, called the *C*-matrix, according to equation (1):

$$C = [I + \text{SDF}]^{-1} \qquad (1)$$

where *I* is the identity matrix. The corrected, or in-band, signal is the dot product of matrix *C* and the measured signal, equation (2):

$$S_{\text{IB}} = C S_{\text{Measured}}. \qquad (2)$$

Figure 19 shows the ratio between the stray light corrected and uncorrected signals for IRIS measurements of the integrating sphere calibration source and of a model lunar irradiance (see section 4).

3.3.3. Wavelength. The laser line spectra also formed the basis of a wavelength scale. The pixel location of both the centroid of each laser line and the peak of a Gaussian fit to the laser line were associated with the LSA-measured wavelengths. The data were interpolated to give a wavelength for each pixel. Differences between the IRIS centroid and peak wavelengths and the LSA-measured wavelengths are shown in figure 20 as differences from the vendor wavelength scale.

The wavelength scale was routinely checked during calibrations by introducing Hg, Ar, and Xe pen lamps into the calibration source sphere. Emission lines were measured that were symmetric and separated enough from neighboring lines to avoid confusion; a total of 11 emission lines with peak emissions ranging from 365.02 nm to 992.32 nm [30]. The measured emission lines were fit to Gaussian line shapes. The fit value of the peak was taken as the pixel location of the emission line. The resultant wavelength as a function of pixel number was fit to a second order polynomial; fit residuals were ±0.05 nm. Differences from vendor-provided wavelengths are also shown in figure 20.

There is good agreement to the wavelength scale correction using the LSF peaks and centroids or the pen lamps from 475 nm to 1100 nm. Below 475 nm the centroid-based correction data begin to diverge from the peak-based wavelength corrections. Below 375 nm, the calculated pen lamp and LSF peak wavelength correction also begin to diverge. This may be caused by a shoulder in the 365 nm Hg line skewing the fit. We continue to investigate the cause of these differences as they lead to a larger uncertainty in the wavelength scale at the blue end of the spectrum. The wavelength derived using the peak wavelengths is currently used. Taking the partial derivative of IRIS's responsivity to wavelength we can determine the relative wavelength sensitivity coefficients which are given in figure 21.

3.3.4. Temperature sensitivity. Thermocouple TC4 is located on the input to the spectrograph. The ratios to the mean of four repeat measurements of IRIS's responsivity at different TC4 temperature readings are shown in figure 22. IRIS temperature sensitivity coefficients derived from the partial derivative of the responsivity to temperature from those measurements are given in figure 23. Figure 24 shows the temperature-corrected repeat measurements of IRIS's responsivity ratioed to the mean and figure 25 shows the impact of the temperature correction on the measurement uncertainty.

3.3.5. Temporal stability. The irradiance scale is held by a transfer standard (TS) spectrograph and transferred to IRIS during calibration (section 3.3.4). It is important that the TS be able to hold the irradiance scale over the course of a deployment. A typical air-LUSI deployment is anticipated to last approximately 2 weeks. To evaluate the temporal stability of the TS, it was left on the calibration bench and was calibrated four times over the course of a month. The calibrations are shown in figure 26 relative to the mean; the standard deviation of the calibrations provided in figure 27 was 0.02% over
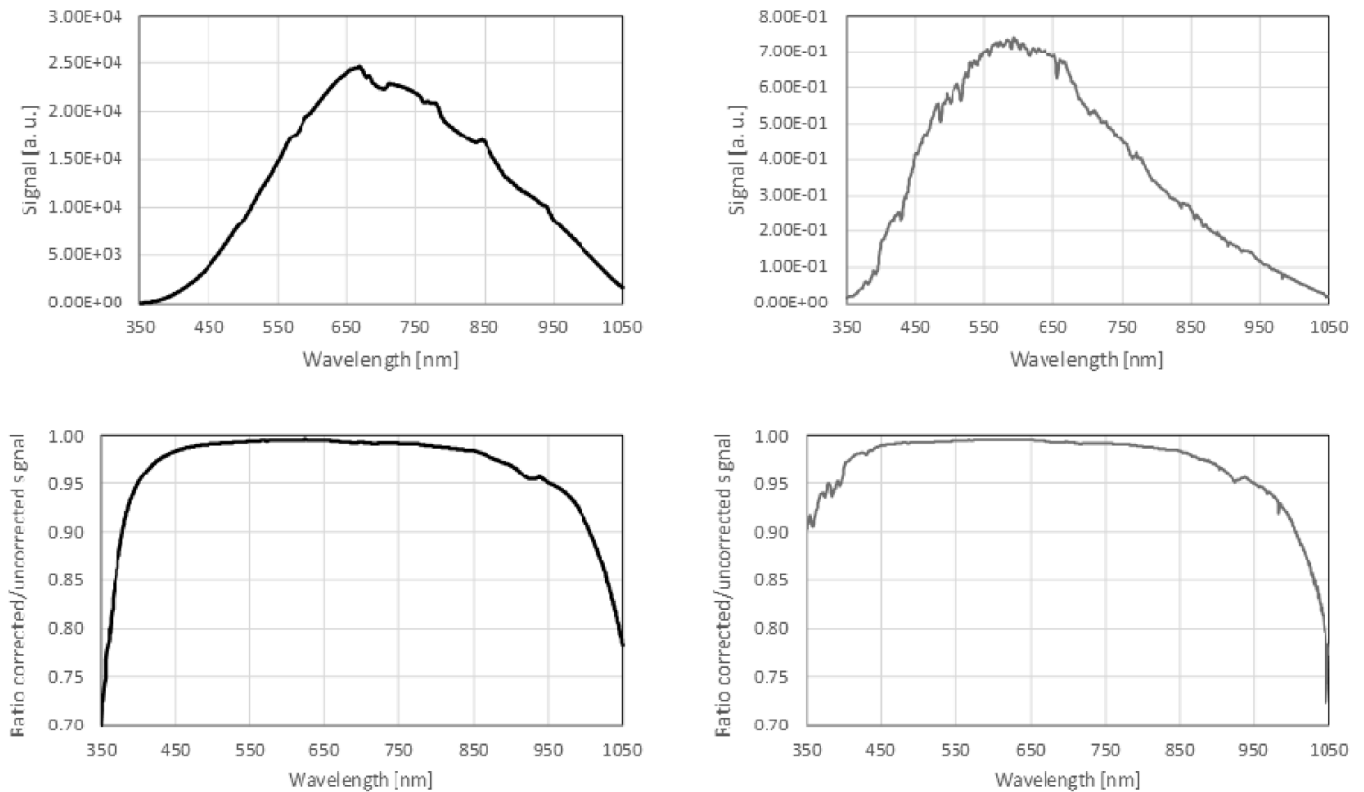
Figure 19. The ratio between IRIS stray light corrected and uncorrected signals: (*l*) the IS calibration source and (*r*) an estimated lunar irradiance spectrum.
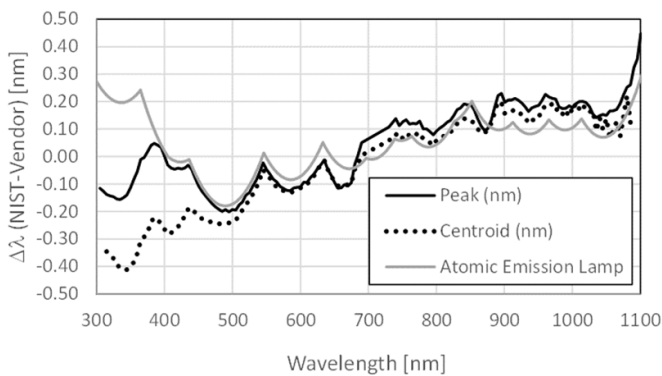

Figure 20. Corrections to the IRIS wavelength scale using the peak and the centroid wavelengths.
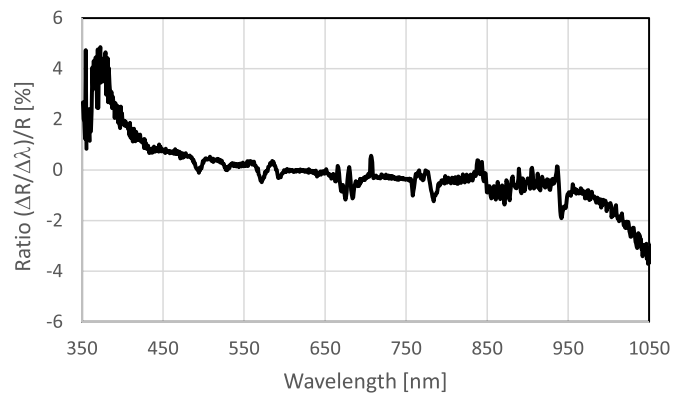

Figure 21. Relative wavelength sensitivity coefficients.

the spectral range from 550 nm to 1050 nm, less than 0.05% from 430 nm to 550 nm, and less than 0.2% from 350 nm to 430 nm.

3.3.6. LED source stability. A typical ER-2 flight is estimated to last 3 h. The stability of the in-flight LED calibration validation source was tested several times over durations ranging from 4 h to 12 h. Figure 28 shows the ratio between the signal from the PD mounted in the wall of the integrating sphere telescope receiver and the LED monitor PD in the Instrument Enclosure.

4. Estimates of the expected signals from in-flight measurements of lunar irradiance

Using the IRIS responsivity and a model of the lunar irradiance, the IRIS signal levels can be estimated. A thorough description of the IRIS calibration procedure will be presented in a future publication; however, a short description of the process will be provided here. A TS spectrograph fiber-coupled to a diffuser head holds the irradiance scale and transfers it to IRIS using a lamp-illuminated ISS. The TS is calibrated against FEL-type irradiance standard lamps traceable to
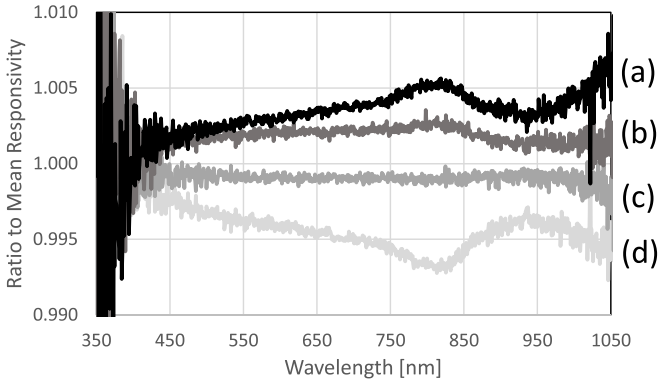
Figure 22. Repeat measurements of IRIS's responsivity uncorrected for TC4 temperatures of 28.5 °C (a), 27.4 °C (b), 26.0 °C (c), and 23.5 °C (d).
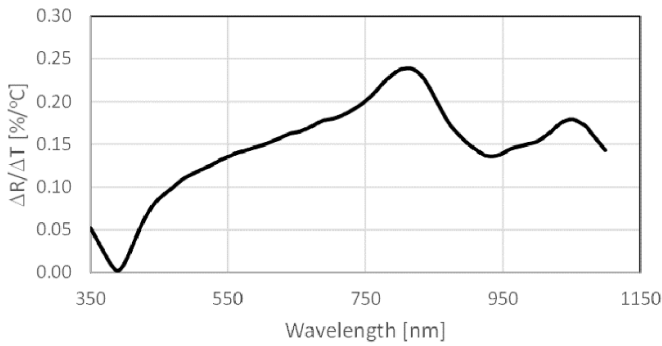

Figure 23. IRIS sensitivity coefficients based on TC4 measurements and their type A standard deviations.
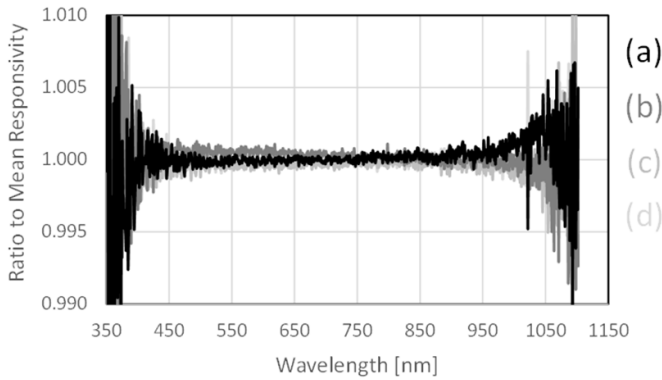

Figure 24. Repeat measurements of IRIS's responsivity corrected for TC4 temperatures of 28.5 °C (a), 27.4 °C (b), 26.0 °C (c), and 23.5 °C (d).

Figure 25. Measurement uncertainty with and without the temperature correction applied.

Figure 26. Temporal stability of IRIS's responsivity.

Figure 27. Measurement uncertainty with and without the temperature correction applied.

primary standard blackbody sources at NIST [31]. To determine the irradiance of the ISS, the TS spectrograph's irradiance head is mounted on a kinematic mount attached to a translation stage at a distance of approximately 0.85 m from the ISS exit aperture. An alignment laser mounted on the faceplate of the ISS is used to center and align the TS spectrograph irradiance head as well as to align the ISS to the IRIS telescope.

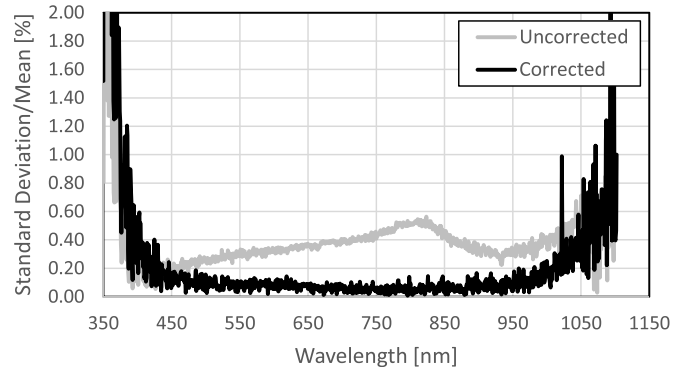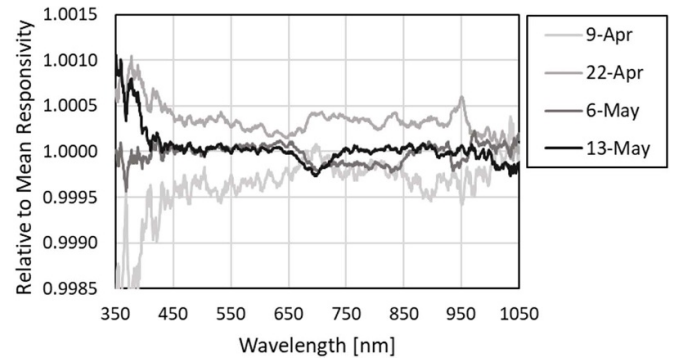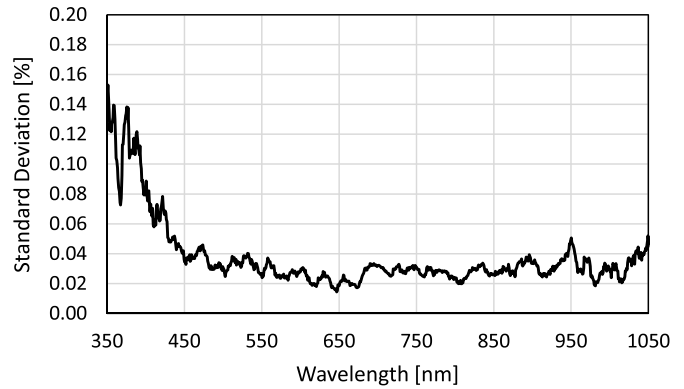Once the irradiance of the ISS was determined, IRIS measured the irradiance from the calibration source at a separation of approximately 12 m. Its responsivity for each element in the detector array at the instrument's focal plane, $R_i(\lambda)$, is calculated using the following equation:

$$R_i(\lambda) = \frac{S_i(\lambda)}{E(\lambda) \times \Delta\tau\,(\mathrm{ms})}, \qquad (3)$$

where $S_i(\lambda)$ is the measured signal, $E(\lambda)$ is the irradiance at the telescope aperture, and $\Delta\tau$ is the detector array's integration time. For this estimate of the expected in-flight signals looking at the Moon, a stray light correction was applied
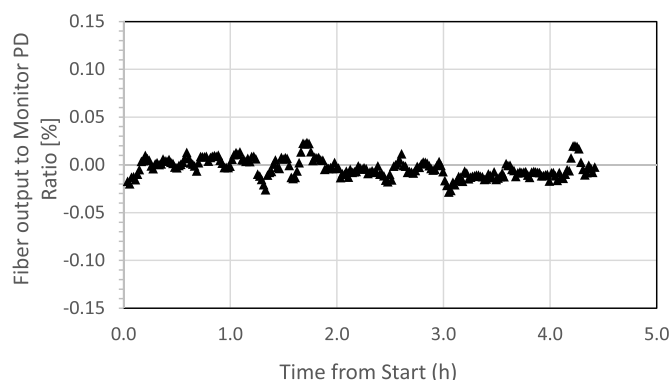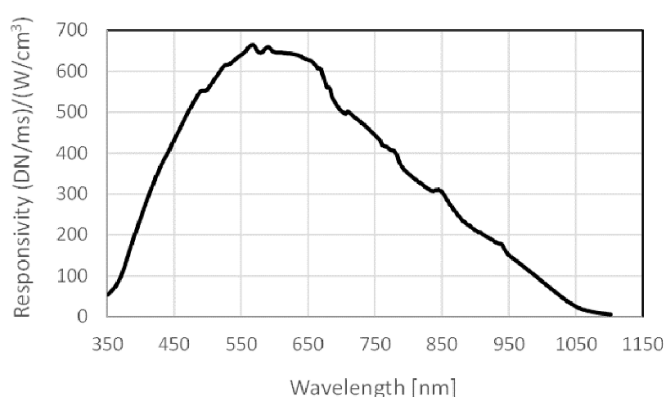
Figure 28. LED stability.
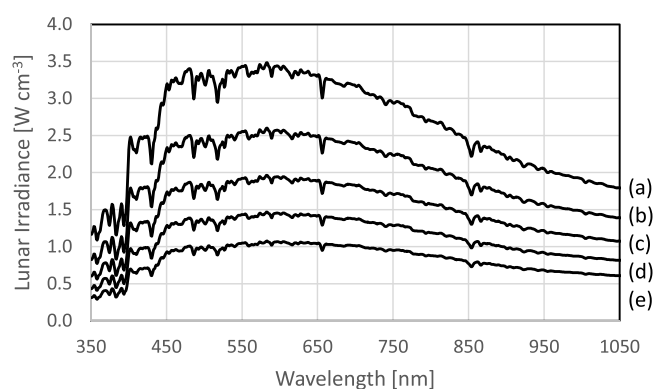

Figure 29. IRIS responsivity.

Figure 30. ROLO-generated lunar irradiances for phase angles seen during 2019 demonstration flight campaign. Modelled phase angles include 10° (a), 21° (b), 34° (c), 46° (d) and 59° (e).

but additional corrections from the influencing variables discussed in section 3 were not applied because they were small. Figure 29 shows IRIS's responsivity.

To ensure the instrument has adequate signal-to-noise, using the IRIS responsivity and the USGS ROLO model of the lunar irradiance, the lunar irradiance signal was estimated for lunar phase angles from 10° to 59°, phase angles expected for a Demonstration Flight campaign that occurred in November 2019. The irradiance estimates are shown in figure 30. Combining these estimates and the responsivity
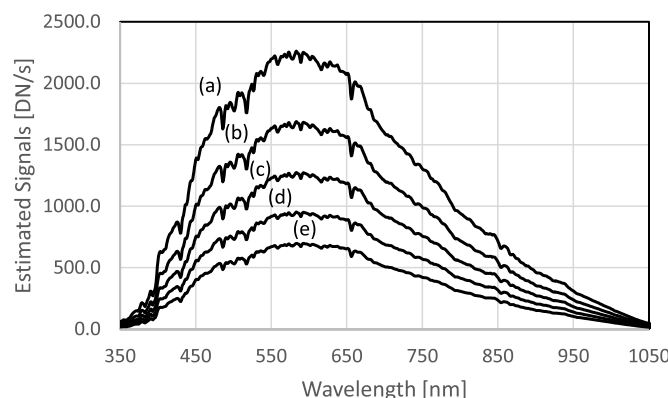

Figure 31. Estimated signals for in-flight lunar irradiance measurements using a 5 s integration time. Signals are estimated for phase angles are 10° (a), 21° (b), 34° (c), 46° (d) and 59° (e).

provides the estimated signals shown in figure 31. Based on the signal estimates, it was determined that a 5 s integration time be incorporated during the 2019 Demonstration Flights to provide adequate signal-to-noise.

5. Summary and conclusions

Air-LUSI is an airborne instrument designed to measure the lunar irradiance from a high-altitude ER-2 aircraft with a combined standard uncertainty of 0.5% or less over the spectral range from 380 nm to 980 nm. The development and characterization of the air-LUSI radiometric subsystem, IRIS, was presented. Characterization tests included many of the variables to be used in the development of an uncertainty budget for IRIS. Using the ROLO model to estimate the at-sensor lunar irradiance, in-flight lunar irradiance signals for phase angles ranging from 10° to 60° were estimated. Pre-deployment of air-LUSI, NASA assessed the Technology Readiness Level of IRIS to be 6.

An Engineering Flight campaign was held in August 2018 to test air-LUSI's functionality under operational conditions, mounted in the body of an ER-2 aircraft and flown at an altitude above 20 km. Following a successful Engineering Flight campaign, a Demonstration Flight campaign was held in November 2019. Results of the Demonstration Flight campaign, including an estimate of the uncertainties in measurements of lunar irradiance, are forth-coming.

Data availability statement

The data that support the findings of this study are available upon reasonable request from the authors.

Acknowledgments

ORCID iDs

Steven E Grantham ⬤ https://orcid.org/0000-0002-8218-512X

Kevin R Turpie ⬤ https://orcid.org/0000-0002-1637-6008

Thomas C Stone ⬤ https://orcid.org/0000-0001-5088-3495

S Andrew Gadsden ⬤ https://orcid.org/0000-0003-3749-0878

Thomas C Larason ⬤ https://orcid.org/0000-0001-5249-6317

Clarence J Zarobila ⬤ https://orcid.org/0000-0003-4547-0754

John T Woodward ⬤ https://orcid.org/0000-0001-7719-3187

Steven W Brown ⬤ https://orcid.org/0000-0003-3561-3934

References

[1] Bacour C, Briottet X, Bréon F-M, Viallefont-Robinet F and Bouvet M 2011 Revisiting pseudo invariant calibration sites (PICS) over sand deserts for vicarious calibration of optical imagers at 20 km and 100 km scales *Remote Sens.* **11** 1166

[2] Tuli F T Z, Pinto C T, Angal A, Xiong X and Helder D 2019 New approach for temporal stability evaluation of pseudo-invariant calibration sites (PICS) *Remote Sens.* **11** 1502

[3] Kieffer H H 1997 Photometric stability of the lunar surface *Icarus* **130** 323–7

[4] Kieffer H H *et al* 2003 On-orbit radiometric calibration over time and between spacecraft using the Moon *Proc. SPIE* **4881** 287–97

[5] Kieffer H H and Stone T C 2005 The spectral irradiance of the moon *Astron. J.* **129** 2887–901

[6] Stone T C and Kieffer H H 2006 Use of the Moon to support on-orbit sensor calibration for climate change measurements *Proc. SPIE* **6296** 62960Y

[7] Wagner S C *et al* 2015 A summary of the joint GSICS-CEOS/IVOS lunar calibration workshop: working towards intercalibration using the Moon as a transfer target *Proc. SPIE* **9639** 96390Z–1

[8] Wagner S C 2017 *Second Joint GSICS/IVOS Lunar Calibration Workshop* ed S C Wagner (Xi'an)

[9] Stone T C, Kieffer H, Lukashin C and Turpie K 2020 The Moon as a climate-quality radiometric calibration reference *Remote Sens.* **12** 1837

[10] Stone T C 2008 Radiometic calibration stability and intercalibration of solar-band instruments in orbit using the Moon *Proc. SPIE* **7081** 70810X

[11] Stone T 2010 Stellar calibration of the ROLO lunar radiometric reference *SPIE Optical Engineering + Applications* vol 7807 (SPIE) (https://doi.org/10.1117/12.862141)

[12] Cramer C E, Lykke K R, Woodward J T and Smith A W 2013 Precise measurement of lunar spectral irradiance at visible wavelengths *J. Res. Natl Inst. Stand. Technol.* **118** 396–402

[13] Cramer C E *et al* 2013 A novel apparatus to measure reflected sunlight from the Moon *Proc. SPIE* **8867** 8867OW

[14] Zarobila C J, Grantham S, Brown S W, Woodward J T, Maxwell S E, Defibaugh D R, Larason T C and Turpie K R 2020 Optical and mechanical design of a telescope for lunar spectral irradiance measurements from a high-altitude aircraft *Rev. Sci. Instrum.* **91** 094505

[15] Gibbs Yvonne NASA (available at: https://www.nasa.gov/centers/armstrong/news/FactSheets/FS-046-DFRC.html) (Accessed 16 March 2022)

[16] NASA 2002 *ER-2 Airborne Laboratory Experimenter Handbook* (Edwards, CA: National Aeronautics and Space Administration, Dryden Flight Research Center)

[17] Swingler C 2011 (available at: https://support.steadfast.net/knowledgebase/article/View/88/3/correcting-windows-clock-drift-under-high-cpu-conditions) (Accessed 16 March 2022)

[18] Newton A, Cataford A, Maxwell S E, Gadsden S A and Turpie K 2020 Air-LUSI: development of a pointing and tracking control system for lunar spectral measurements *Acta Astronaut.* **176** 558–66

[19] Cataford A *et al* 2018 Air-LUSI: estimation, filtering, and PID tracking simulation *IEEE Canadian Conf. on Electrical and Computer Engineering (CECE)* (*Quebec City, Quebec, Canada*) (https://doi.org/10.1109/CCECE.2018.8447850)

[20] Cataford A, Gadsden S A and Turpie K R 2020 Air-LUSI: a robotic telescope design for lunar spectral measurements *Adv. Space Res.* **65** 2315–23

[21] Kirby R K 1956 Thermal expansion of polytetrafluoroethlene (Teflon) from −190 °C to +300 °C *J. Res. Natl Bur. Stand.* **57** 91–94

[22] Ball C P, Levick A P, Woolliams E R, Green P D, Dury M R, Winkler R, Deadman A J, Fox N P and King M D 2013 Effect of polytetrafluoroethylene (PTFE) phase transition at 19 °C on the use of spectralon as a reference standard for reflectance *Appl. Opt.* **52** 4806–12

[23] Feller J R 2012 Dependence of multi-layer insulation thermal performance on interstitial gas pressure *AIP Conf. Proc.* **1434** 47

[24] Thompson A and Chen H M 1994 Beam III: a linearity measurement instrument for optical detectors *J. Res. Natl Inst. Stand. Technol.* **99** 751–5

[25] Yoon H W, Butler J J, Larason T C and Eppeldauer G P 2003 Linearity of InGaAs photodiodes *Metrologia* **40** S154–S158

[26] White D R, Clarkson M T, Saunders P and Yoon H W 2008 A general technique for calibrating indicating instruments *Metrologia* **45** 199–210

[27] Nevas S, Wübbeler G, Sperling A, Elster C and Teuber A 2012 Simultaneous correction of bandpass and stray-light effects in array spectroradiometer data *Metrologia* **49** S43–S47

[28] Zong Y, Brown S W, Johnson B C, Lykke K R and Ohno Y 2006 Simple spectral stray light correction method for array spectroradiometers *Appl. Opt.* **45** 1111–9

[29] Kostkowski H J (ed) 1997 Spectral scattering *Reliable Spectroradiometry* (La Plata, MD: Spectroradiometry Consulting) pp 57–87

[30] Sansonetti J E and Martin W C 2005 NIST standard reference database 108: handbook of basic atomic spectroscopic data *J. Phys. Chem. Ref. Data* **34** 1559–2259

[31] Yoon H W and Gibson C E 2011 Spectral irradiance calibrations *Natl. Inst. Stand. Technol. Spec. Publ.* vol SP250-43 (Washington, DC: US Government Printing Office) p 123